IEEE Access
Multidisciplinary | Rapid Review | Open Access Journal

Date of publication xxxx 00, 0000, date of current version xxxx 00, 0000.

Digital Object Identifier 10.1109/ACCESS.2017.Doi Number

Non-ionizing Label-free Photoacoustic Imaging of Bones

Eun-Yeong Park[1,§], Donghyun Lee[1,§], Changho Lee[2,*], and Chulhong Kim[1,*], Senior Member, IEEE

[1]Departments of Electrical Engineering, Creative IT Engineering, Mechanical Engineering, and Medical Device Innovation Center, Pohang University of Science and Technology (POSTECH), Pohang 37673, Republic of Korea
[2]Department of Nuclear Medicine, Chonnam National University Medical School and Hwasun Hospital, Chonnam 58128, Republic of Korea

[§]These authors contributed equally to this work.

Corresponding authors: Chulhong Kim (e-mail: chulhong@postech.edu) and Changho Lee (e-mail: ch31037@jnu.ac.kr)

This research was supported by the National Research Foundation of Korea (NRF) grant funded by the Korea government (Ministry of Science and ICT; MSIT) (No. NRF-2019R1A2C2006269), a grant of the Korea Health Technology R&D Project through the Korea Health Industry Development Institute (KHIDI), funded by the Ministry of Health & Welfare, Republic of Korea (grant number: HI15C1817), and Basic Science Research Program through the National Research Foundation of Korea (NRF) funded by the Ministry of Education (2020R1A6A1A03047902).

ABSTRACT X-ray based radiography, the main modality for diagnostic imaging of bone structures and fractures, provides sensitive images, but it inherently involves potentially harmful X-ray exposure. As non-ionizing alternatives, various optical imaging methods have been explored. Here, we demonstrate non-ionizing, label-free, multispectral photoacoustic (PA) imaging of bones in small animals *in vivo*, *in situ*, and *ex vivo*. Using near-infrared light excitation and acoustic detection, the spine and ribs were successfully visualized in high-resolution PA images. PA 3D volume images of the spine and ribs were clearly visualized together with blood vessels and several organs including the spleen, liver, and cecum, without using any exogenous contrast agent nor ionizing radiation. Quantification results of multispectral PA signals from blood vessels and bones were in good agreement with their absorption coefficients. Further, a rib fracture was photoacoustically imaged. Our results demonstrate PA imaging's potential as a non-ionizing and label-free technique for imaging bone tissues.

INDEX TERMS Biomedical imaging, Bone imaging, Diagnostic radiography, Label-free, Non-ionizing radiation, Photoacoustic imaging, X-ray radiography

I. INTRODUCTION

Since Röntgen discovered X-rays in 1895, X-ray radiography has been extensively developed as a main diagnostic tool in medicine. Significant technical advances have led to a variety of systems for real-time high-resolution 2D radiography and 3D computed tomography (CT) [4, 5]. X-ray radiographs are used to diagnose maladies in almost any part of the body, including the chest (heart and lung), abdomen, spine, brain, teeth, and pediatric growth plates (bone age), and to image and monitor conditions such as sinusitis and fractures [6-12]. X-ray imaging provides particularly high image contrast for organic and inorganic hard target materials, such as bones and metals. Thus, the modality is widely employed in placing implants and determining nerve locations before and after dental implant procedures, in bone fracture and density diagnosis, and in bone fracture internal fixation. However, compared to other diagnostic modalities, such as magnetic resonance imaging (MRI) and ultrasound (US) imaging, X-ray imaging confronts particular limitations, including weak soft tissue contrast, the provision of only structural information, the use of ionizing radiation, and the difficulty of detecting early microscopic lesions.

Currently, various studies on bone imaging have been conducted using non-ionizing optical imaging techniques, such as bioluminescence imaging, fluorescence imaging, and diffuse optical tomography. Cowey *et al.* monitored bone metastasis in mice with bioluminescent imaging and achieved a sensitivity of 100%, a specificity of 80-90%, and an accuracy of 90-96% compared to histological analysis [13]. Bao *et al.* developed bone-specific pamidronate conjugated near-infrared fluorophores that can provide fluorescence images of the chest, bone, and spine [14]. Niska *et al.* monitored bacterial burden and neutrophil infiltration during orthopedic implant infections, using complementary fluorescence,

This article has been accepted for publication in a future issue of this journal, but has not been fully edited. Content may change prior to final publication. Citation information: DOI 10.1109/ACCESS.2020.3020559, IEEE Access

bioluminescence, and X-ray combined imaging [15]. Xu *et al*. acquired optical absorption and scattering images of chicken bones and human finger joints using diffuse optical tomography [16]. However, exogenous contrast agents are unavoidably required for fluorescence imaging in bones, and these pure optical modalities suffer from relatively low resolution in deep tissues. As for non-optical techniques, US has drawn attention for imaging bone surfaces or joint/bone inflammation thanks to its radiation-free and real-time imaging capability [17-19]. There still remain challenges, however, that morphological features including acoustic shadow behind bone and thickness of bone surface are highly dependent on the orientation of US probe with respect to imaging anatomy and functional features on inflammation such as microvasculature are less sensitive in US images [20, 21].

Photoacoustic (PA) imaging is an optical- and acoustic-based hybrid biomedical imaging technique that can noninvasively provide high-resolution optical images of biological tissues [22-28]. In principle, materials that absorb pulsed light generate US signals through thermal expansion, and the generated US signals are detected by US transducers. Therefore, fruitful optical contrast with high US resolution can be obtained, even in deep tissues. Aforementioned limitations on US bone imaging can be overcome using PA technique by capturing acoustic signal generated from optical absorbers such as blood (hemoglobin) and bone, not the reflected signal from different tissue layers. Because acoustic signal is generated from bone itself, there are little or no dependencies on probe orientation, angle, and operator. In addition, PA imaging is intrinsically sensitive to oxygenated and deoxygenated hemoglobin and thus can provide not only hyper-vascularization but also hypoxia which are hallmarks of joint/bone inflammation. To visualize bone structures in live animals, Fehm *et al*. developed an *in vivo* whole-body PA scanner that can provide volumetric PA images, and used it to visualize the spine of a mouse [29]. Lee *et al*. acquired PA and US combined images of dental implants in a porcine jawbone and visualized the structure of a jawbone, implants, and soft tissues [30]. Thella *et al*. conducted a simulation study on PA diagnosis for various types of bone including cancerous bone and bone marrow [31]. Wood *et al*. monitored oxygen saturation of murine bone marrow based on PA technique to assess leukemic disease progression [32].

Here, we demonstrate label-free high-resolution non-ionizing PA imaging of bones in mice. We have successfully acquired multispectral PA images of bone tissues, including ribs and spines, *in vivo*, *in situ*, and *ex vivo*. Further, the PA results are compared with X-ray CT images. In addition, we have photoacoustically imaged broken ribs. Our results indicate that PA imaging can potentially be a useful tool to image bone structures and maladies in preclinical and clinical settings.

II. MATERIALS AND METHODS

A. ACOUSTIC-RESOLUTION PHOTOACOUSTIC MACROSCOPY

To acquire PA images of bone structures in mice, we utilized an acoustic-resolution photoacoustic macroscopy (AR-PAM) system (Figure 1). The AR-PAM system uses a Q-switched Nd:YAG laser (532 nm; SLII-10, Continuum, USA) and a tunable optical parametric oscillator (OPO) laser (Surelite OPOPLUS, Continuum, USA) for PA excitation. The PA excitation laser provides wavelengths adjustable from 680 nm to 2500 nm, with a pulse width of 5 ns and a repetition rate of 10 Hz. Optical wavelengths of 532 nm, 680 nm, and 850 nm were used for label-free *in vivo*, *in situ*, and *ex vivo* PA imaging, and the optical wavelength of 680 nm was used to monitor a broken rib cage. The PA excitation beam is delivered to a conical lens and a custom-made optical condenser through N-BK7 best form lenses (LBF-254-150, Thorlabs, USA) and 90-angle prisms (PS908, Thorlabs, USA) to make a dark-field ring-shaped beam on the imaging targets. The pulse energy of the laser beam used for PA imaging is ~4 mJ/cm^2, which is well below the American National Standards Institute (ANSI) laser safety limits. To detect the generated PA signal, a single-element focused US transducer with a 5 MHz central frequency (V308, Olympus NDT, USA) and a pulser/receiver (5072PR, Olympus NDT, USA) are used. The US transducer is placed in a custom-made optical condenser at a distance of 1 inch from the imaging target, which is the focal length of the US transducer. The detected PA signals are recorded with a digital oscilloscope (MSO 5204, Tektronix, USA) at 50 MHz sampling rate. For US signal coupling, a custom-made water bath covered with a transparent polyvinyl chloride film is placed between the optical condenser and the imaging target. 3D volumetric PA images are acquired by moving the conical lens and the custom-made optical condenser via two stepper motors in a range of 60 mm (X) × 40 mm (Y) × 30 mm (Z). The image acquisition time is about 40 minutes and the axial and lateral resolutions of the AR-PAM system are 145 μm and 590 μm, respectively.

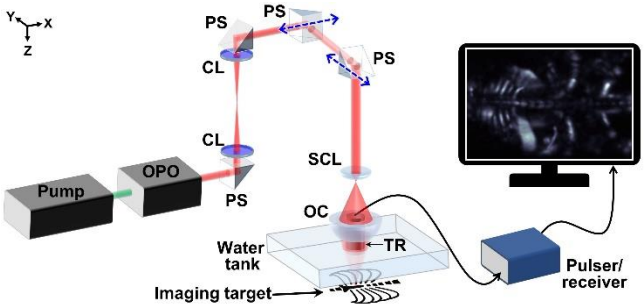

Figure 1. Schematic of acoustic-resolution photoacoustic macroscopy. Blue dashed arrows represent the scanning axes. OPO, optical parametric oscillator; PS, prism; CL, collimating lens; SCL, spherical conical lens; OC, optical condenser; TR, ultrasound transducer.

This article has been accepted for publication in a future issue of this journal, but has not been fully edited. Content may change prior to final publication. Citation information: DOI 10.1109/ACCESS.2020.3020559, IEEE Access

B. MURINE COMPUTED TOMOGRAPHY

To acquire X-ray CT images of live mice, we used a low dose CT system (Quantum FX microCT, PerkinElmer Inc, USA). The CT system provides a photon energy of 90 kV at 0.2 mA, and has focal spot of 5 ~ 30 μm. A 127 μm pixel 14-bit X-ray flat panel detector is used to capture CT signals. The field of view (FOV) of the CT system is cylindrical with a diameter of 34 mm and a length of 60 mm. For *in vivo* mouse CT imaging, the mouse was anesthetized by a vaporized-isoflurane system (XGI-8, PerkinElmer Inc, USA).

C. ANIMAL PREPARATION

Six-week old female normal balb/c mice (weight: ~ 25 g) were prepared for PA bone imaging. All animal experimental procedures were conducted following the laboratory animal protocol approved by the Institutional Animal Care and Use Committee (IACUC) of the Pohang University of Science and Technology (POSTECH) and in accordance with the National Institutes of Health Guide for the Care and Use of Experimental Animals. For *in vivo* PA and CT imaging, the mouse was anesthetized with a vaporized-isoflurane system (1L/min of oxygen and 0.75% isoflurane). Then the mouse was sacrificed for *in situ* imaging with and without skins, and for *ex vivo* imaging. To image bone fracture, we initially euthanized the animal, broke ribs, and then photoacoustically imaged the fractured rib cage *in situ*.

D. IMAGE SEGMENTATION

For a quantitative analysis, we segmented the PA images into blood vessels, bones, organs (including spleen, cecum, and liver), and background regions. For each region, a polygonal region-of-interest (ROI) was manually created on a maximum amplitude projection (MAP) image, and then a binary mask was created from pixels inside the ROI with values greater than a manually defined threshold. Then, using 3D PHOVIS software developed in [33], each volume region was rendered with different color maps of hot-, blue-, copper-, and gray-scale for blood vessels, bones, organs, and background regions, respectively.

III. RESULT AND DISCUSSION

In vivo CT images of a mouse were acquired to compare with the PA images. Bones and lungs, lending themselves well to X-ray radiography, are clearly visualized in the CT volumetric image (Figure 2a) and cross-sectional images (Figure 2b-d). Gas-containing organs such as the intestine and cecum can be read based on anatomical information. Other internal structures, including the liver, spleen, and blood vessel are invisible and typically require a radiocontrast agent to be seen.

PA images were then acquired under different conditions, such as *in vivo*, *in situ* with and without skin, and *ex vivo*. Figure 3 shows label-free PA MAP images and 3D volume-rendered images captured at various optical wavelengths. A gray scale represents the PA amplitude of the background, a

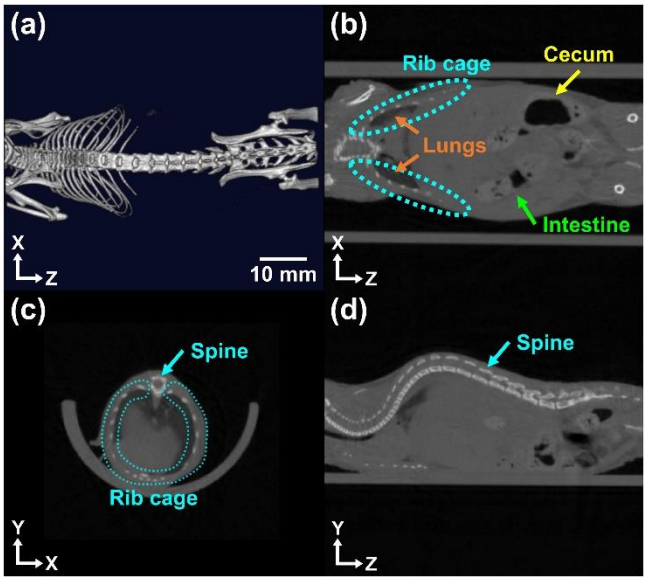

Figure 2. ***In vivo*** **CT images of a mouse. (a) 3D volume, (b) coronal plane, (c) axial plane, and (d) sagittal plane.**

blue scale indicates the PA amplitude in bones (ribs and backbone), a hot scale (from deep red to yellow) shows the PA amplitude in blood vessels, and a copper scale indicates the PA amplitude in organs (spleen, cecum, and liver). Movie clips of 3D volume-rendered PA images are presented in Supplementary Video 1-9. The 532 nm *in vivo* PA MAP image (Figure 3aii) shows primarily blood vessels near the skin. As the optical wavelength becomes longer, stronger PA signals are obtained from the ribs and spine, located deeper below the skin than the blood vessels (Figure 3a iii and iv). This result demonstrates that the longer the optical wavelength, the smaller the optical scattering in the tissue, resulting in deeper light transmission. Additionally, the optical absorption coefficient of hemoglobin in the near-infrared region (680 nm and 850 nm) is less than that in the 532 nm wavelength. Therefore, the PA signals from blood vessels near the skin are weaker with near-infrared illumination than those at 532 nm. Next, we acquired *in situ* PA MAP images (Figure 3b). Compared to the *in vivo* PA MAP images with 532 nm excitation, the PA signal from blood vessels in dead mice is decreased (Figure 3bii). After death, the heart stops beating and the capillary circulation ceases, and blood vessels near skin become less visible in the PA MAP images. As blood drains into the large vessels or settles in the lowermost vessels by gravity, large blood vessels near the thigh and the tail become more visible [34]. The spine and the rib cage are clearly visible in the PA MAP images captured at optical wavelengths of 680 nm and 850 nm (Figure 3b iii and iv).

After skin removal, the spine and the rib cage are more clearly visible (Figure 3c). In the PA MAP with 532 nm excitation (Figure 3cii), blood vessels are invisible and internal organs, including the liver, spleen, and cecum, are seen. Penetration depth gets deeper as the optical wavelength gets longer [35], and thus the spine, rib cage, and large arteries near

This article has been accepted for publication in a future issue of this journal, but has not been fully edited. Content may change prior to final publication. Citation information: DOI 10.1109/ACCESS.2020.3020559, IEEE Access

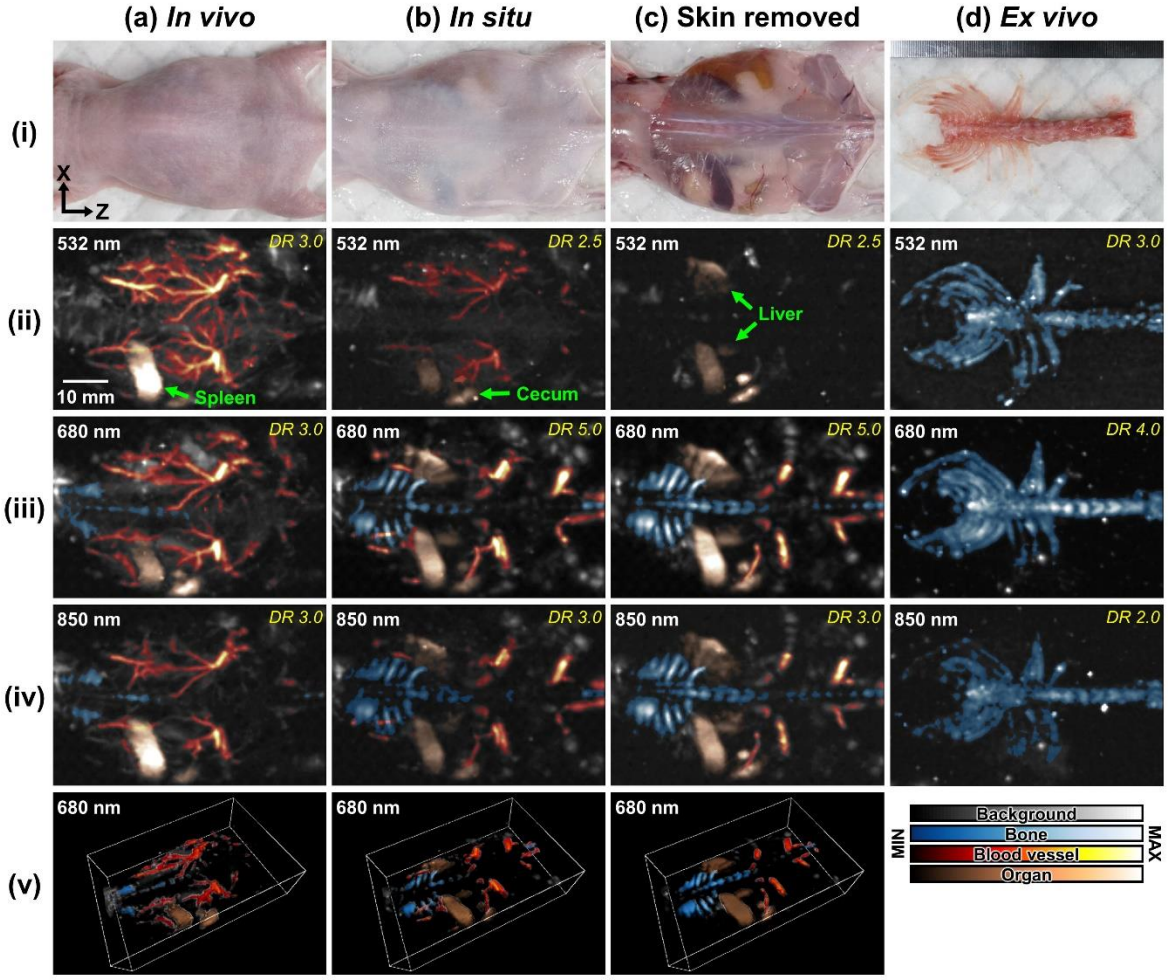

Figure 3. **(i) Photographs of mouse in different conditions: (a) *in vivo*, (b) *in situ*, (c) skin removed, and (d) *ex vivo*, and corresponding label-free PA (ii-iv) MAP and (v) 3D volume-rendered images captured using different excitation laser wavelengths. The gray-, blue-, hot-, and copper-scale images respectively represent PA amplitudes in the background, bone, blood vessels, and organs. The minimum and maximum values of the colormaps are 0 and DR, respectively. MAP, maximum amplitude projection; PA, photoacoustic; DR, dynamic range.**

the thigh and tail are clearly visible (Figure 3c iii and iv). Next, we acquired PA MAP images of the spine and rib cage after they were removed from the body (Figure 3d). As with the *in situ* and skin-removed conditions, the spine and rib cage are more clearly visualized, and the nodes of the spine appear in the PA MAP images with 680 nm and 850 nm excitation. PA signal of *ex vivo* bones obtained at 532 nm (Figure 3dii) are weaker than that at 680 nm (Figure 3diii) despite higher absorbance (TABLE I). This might be due to strong optical scattering in remaining biological tissues on excised bones at

TABLE I. Absorption coefficients of bone and blood at 532, 680, and 850 nm wavelengths. Bone data are from [1] and [2], and blood data are calculated using data from [3].

Wavelength	532 nm	680 nm	850 nm
Bone [1]	1.11 cm^{-1}	0.48 cm^{-1}	0.20 cm^{-1}
Bone [2]	-	0.28 cm^{-1}	0.27 cm^{-1}
Artery (SO_2 98%)	234.60 cm^{-1}	1.71 cm^{-1}	5.63 cm^{-1}
Vein (SO_2 70%)	229.66 cm^{-1}	4.91 cm^{-1}	5.08 cm^{-1}

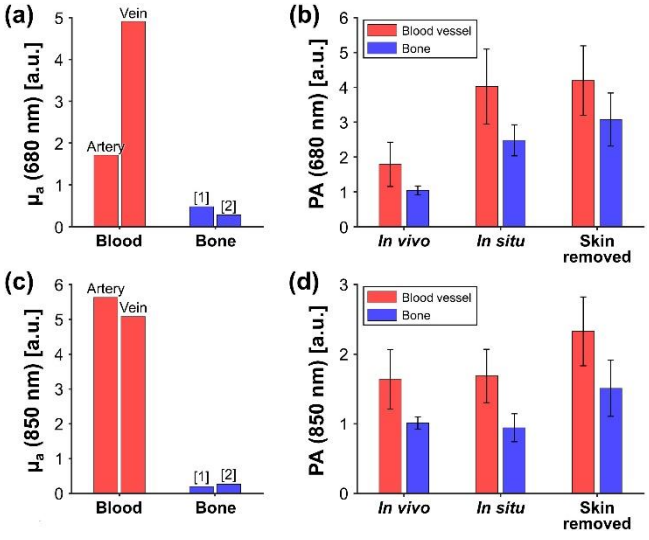

Figure 4. **Absorption coefficients (μ_a) of bone and blood at 680 nm (a) and 850 nm (c). PA amplitudes in bone and blood vessels at (b) 680 nm and (d) 850 nm, for different mouse conditions.**

This article has been accepted for publication in a future issue of this journal, but has not been fully edited. Content may change prior to final publication. Citation information: DOI 10.1109/ACCESS.2020.3020559, IEEE Access

the shorter optical wavelength. Although the bone images are not as clean as in CT images, bone images can be successfully obtained from PA images non-invasively, without using ionizing radiation and any contrast agent. Imaging in the NIR-II window, such as 1064 nm, might contribute to achieving deeper imaging depth.

We further compared multispectral PA signals from bone and blood vessels under *in vivo*, *in situ*, skin-removed, and *ex vivo* conditions (Figure 4b and d) with the absorption coefficients of bone and blood (TABLE I and Figure 4a and c). The quantified PA amplitudes in Figure 4b and d are average signals within each ROI (colored volume data in Figure 3: bone in blue-scale and blood vessel in hot-scale) and their standard deviation. As can be seen, for *in situ* and skin-removed conditions, as capillary circulation collapses and the blood sinks down into the large vessels, PA signals from capillaries near the skin significantly decrease at 532 nm. Correspondingly, compared to the *in vivo* PA signals, PA signals from large vessels near the thigh and the tail greatly increase at 680 nm. With the reduced absorption from blood in dead mice, PA signals from bone markedly increase at 680 nm excitation, to about 2.6 and 2.0 times higher than those at 850 nm in the *in situ* and skin-removed conditions, respectively. These values match well with the absorption coefficients of bone in TABLE I.

To investigate the feasibility of imaging bone fractures, we photoacoustically examined a rib cage fracture in situ. As a control, before the rib were broken, we acquired in situ PA MAP images at 680 nm (Figure 5a), in which the spine and rib cage are clearly visualized. Then, we broke left ribs and repeated the PA imaging experiments. The fractured parts of the ribs in the PA MAP image are clearly visualized at 680 nm (yellow dashed circle region in Figure 5b). Additionally, the ribs and spine are clearly visualized in PA cross-sectional images (Figure 5c), of the red arrow regions in Figure 5b. The B-mode image at line 4 in Figure 5c clearly shows the missing rib signal at the fractured site. These results demonstrate that PA imaging can both show bones and reveal bone fracture without using ionizing radiation.

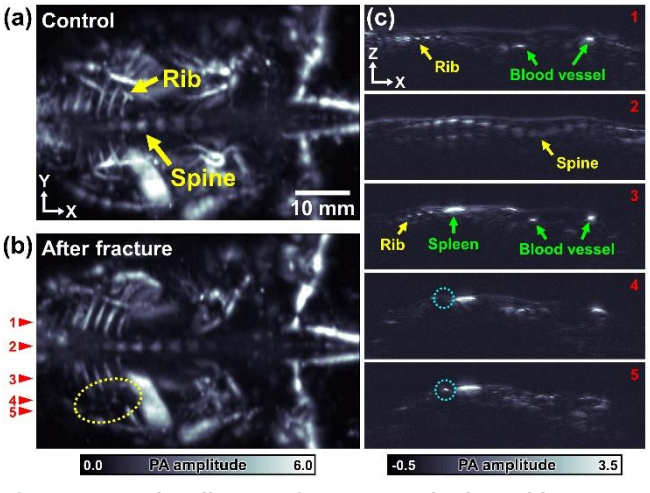

Figure 5. ***In situ*** **rib cage fracture monitoring with 680 nm excitation before (a) and after (b) a fracture. The yellow dotted circle in (b) contains the fracture site. (c) PA cross-sectional images of red arrow regions in (b). The cyan dotted circles in (c) 4 and 5 enclose fractured (missing rib) and normal ribs, respectively.**

IV. CONCLUSION

In this study, we acquired PA bone images of mice *in vivo*, *in situ*, with the skin removed, and *ex vivo*, using an AR-PAM system with optical wavelengths of 532 nm, 680 nm, and 850 nm. Bones, especially the spine and the rib cage, were visualized in PA MAP images with near-infrared wavelengths. Additionally, a rib fracture was imaged at 680 nm. Longer wavelengths reduced image perturbations by veins near the skin and thus showed better images of bones deep below the skin. In addition, because blood flow had ceased in dead mice, large arteries and bones were more clearly visualized. Finally, a rib fracture was successfully visualized with PA imaging. Although PA imaging does not have much higher bone contrast than conventional X-rays, it can provide bone images non-invasively and without using ionizing radiation. PA imaging can also be used for inflammatory arthritis diagnosis and treatment monitoring using strengths that can provide various information such as soft tissue and blood vessel around bones [36, 37]. These results demonstrate that the PA imaging can visualize bones inside the body without ionizing radiation exposure and can be a vital tool for diagnosing bone conditions in orthopedics.

REFERENCES

[1] N. Ugryumova, S. J. Matcher, and D. P. Attenburrow, "Measurement of bone mineral density via light scattering," *Physics in Medicine & Biology*, vol. 49, no. 3, p. 469, 2004.
[2] M. Firbank, M. Hiraoka, M. Essenpreis, and D. Delpy, "Measurement of the optical properties of the skull in the wavelength range 650-950 nm," *Physics in Medicine & Biology*, vol. 38, no. 4, p. 503, 1993.
[3] S. Prahl, "Tabulated molar extinction coefficient for hemoglobin in water," *http://omlc. ogi. edu/spectra/hemoglobin/summary. html*, 1999.
[4] G. N. Hounsfield, "Computerized transverse axial scanning (tomography): Part 1. Description of system," *The British journal of radiology*, vol. 46, no. 552, pp. 1016-1022, 1973.
[5] W. C. Röntgen, "On a new kind of rays," *Science*, vol. 3, no. 59, pp. 227-231, 1896.
[6] A. Abdelkarim, "Cone-Beam Computed Tomography in Orthodontics," *Dentistry journal*, vol. 7, no. 3, p. 89, 2019.
[7] E. Eisenhuber, C. M. Schaefer-Prokop, H. Prosch, and W. Schima, "Bedside chest radiography," *Respiratory Care*, vol. 57, no. 3, pp. 427-443, 2012.
[8] S. M. Garn, "Radiographic atlas of skeletal development of the hand and wrist," *American journal of human genetics*, vol. 11, no. 3, p. 282, 1959.
[9] F. Macellari, M. Paciaroni, G. Agnelli, and V. Caso, "Neuroimaging in intracerebral hemorrhage," *Stroke*, vol. 45, no. 3, pp. 903-908, 2014.
[10] D. Paramythiotis, K. Kofina, V. Papadopoulos, and A. Michalopoulos, "Diagnostic colonoscopy leading to perforated appendicitis: a case report and systematic literature review," *Case reports in gastrointestinal medicine*, vol. 2016, 2016.
[11] M. Rodrigues, J. Nunes, S. Figueiredo, A. M. de Campos, and A. F. Geraldo, "Neuroimaging assessment in Down syndrome: a pictorial review," *Insights into imaging*, vol. 10, no. 1, p. 52, 2019.

[12] Y. X. J. Wáng, M. Deng, L.-C. He, M. N. Che-Nordin, and F. R. Santiago, "Osteoporotic vertebral endplate and cortex fractures: a pictorial review," *Journal of orthopaedic translation*, 2018.
[13] S. Cowey *et al.*, "Breast cancer metastasis to bone: evaluation of bioluminescent imaging and microSPECT/CT for detecting bone metastasis in immunodeficient mice," *Clinical & Experimental Metastasis*, vol. 24, no. 5, p. 389, 2007/05/31 2007, doi: 10.1007/s10585-007-9076-8.
[14] K. Bao *et al.*, "Charge and hydrophobicity effects of NIR fluorophores on bone-specific imaging," *Theranostics*, vol. 5, no. 6, p. 609, 2015.
[15] J. A. Niska *et al.*, "Monitoring bacterial burden, inflammation and bone damage longitudinally using optical and μCT imaging in an orthopaedic implant infection in mice," *PloS one*, vol. 7, no. 10, p. e47397, 2012.
[16] Y. Xu, N. Iftimia, H. Jiang, L. L. Key, and M. B. Bolster, "Imaging of in vitro and in vivo bones and joints with continuous-wave diffuse optical tomography," *Optics Express*, vol. 8, no. 7, pp. 447-451, 2001.
[17] K. Yokota, T. Tsuzuki Wada, Y. Akiyama, and T. Mimura, "Detection of synovial inflammation in rheumatic diseases using superb microvascular imaging: Comparison with conventional power Doppler imaging," *Modern Rheumatology*, vol. 28, no. 2, pp. 327-333, 2018/03/04 2018, doi: 10.1080/14397595.2017.1337288.
[18] G. Renaud, P. Kruizinga, D. Cassereau, and P. Laugier, "In vivo ultrasound imaging of the bone cortex," *Physics in Medicine & Biology*, vol. 63, no. 12, p. 125010, 2018/06/12 2018, doi: 10.1088/1361-6560/aac784.
[19] A. K. P. Lim, K. Satchithananda, E. A. Dick, S. Abraham, and D. O. Cosgrove, "Microflow imaging: New Doppler technology to detect low-grade inflammation in patients with arthritis," *European Radiology*, vol. 28, no. 3, pp. 1046-1053, 2018/03/01 2018, doi: 10.1007/s00330-017-5016-4.
[20] S. Konisti, S. Kiriakidis, and E. M. Paleolog, "Hypoxia—a key regulator of angiogenesis and inflammation in rheumatoid arthritis," *Nature Reviews Rheumatology*, vol. 8, no. 3, pp. 153-162, 2012/03/01 2012, doi: 10.1038/nrrheum.2011.205.
[21] I. Hacihaliloglu, "Ultrasound imaging and segmentation of bone surfaces: A review," *TECHNOLOGY*, vol. 05, no. 02, pp. 74-80, 2017, doi: 10.1142/s2339547817300049.
[22] W. Choi, E.-Y. Park, S. Jeon, and C. Kim, "Clinical photoacoustic imaging platforms," *Biomedical engineering letters*, vol. 8, no. 2, pp. 139-155, 2018.
[23] S. Park, U. Jung, S. Lee, D. Lee, and C. Kim, "Contrast-enhanced dual mode imaging: photoacoustic imaging plus more," *Biomedical engineering letters*, vol. 7, no. 2, pp. 121-133, 2017.
[24] C. Kim and Z. Chen, "Multimodal photoacoustic imaging: systems, applications, and agents," *Biomedical Engineering Letters*, vol. 8, no. 2, pp. 137-138, 2018/05/01 2018, doi: 10.1007/s13534-018-0071-6.
[25] H. Jung *et al.*, "A peptide probe enables photoacoustic-guided imaging and drug delivery to lung tumors in K-rasLA2 mutant mice," *Cancer research*, vol. 79, no. 16, pp. 4271-4282, 2019.
[26] J. W. Baik, J. Y. Kim, S. Cho, S. Choi, J. Kim, and C. Kim, "Super Wide-Field Photoacoustic Microscopy of Animals and Humans In Vivo," *IEEE Transactions on Medical Imaging*, vol. 39, no. 4, pp. 975-984, 2020.
[27] J. Kim, J. Y. Kim, S. Jeon, J. W. Baik, S. H. Cho, and C. Kim, "Super-resolution localization photoacoustic microscopy using intrinsic red blood cells as contrast absorbers," *Light: Science & Applications*, vol. 8, no. 1, pp. 1-11, 2019.
[28] W. Choi and C. Kim, "Toward in vivo translation of super-resolution localization photoacoustic computed tomography using liquid-state dyed droplets," *Light: Science & Applications*, vol. 8, no. 1, p. 57, 2019/06/25 2019, doi: 10.1038/s41377-019-0171-9.
[29] T. F. Fehm, X. L. Deán-Ben, S. J. Ford, and D. Razansky, "In vivo whole-body optoacoustic scanner with real-time volumetric imaging capacity," *Optica*, vol. 3, no. 11, pp. 1153-1159, 2016.
[30] D. Lee, S. Park, W.-C. Noh, J.-S. Im, and C. Kim, "Photoacoustic imaging of dental implants in a porcine jawbone ex vivo," *Optics letters*, vol. 42, no. 9, pp. 1760-1763, 2017.
[31] A. K. Thella, J. Rizkalla, A. Helmy, V. K. Suryadevara, P. Salama, and M. Rizkalla, "Non-invasive photo acoustic approach for human bone diagnosis," *Journal of Orthopaedics*, vol. 13, no. 4, pp. 394-400, 2016/12/01/ 2016, doi: https://doi.org/10.1016/j.jor.2016.07.004.
[32] C. Wood, K. Harutyunyan, D. R. T. Sampaio, M. Konopleva, and R. Bouchard, "Photoacoustic-based oxygen saturation assessment of murine femoral bone marrow in a preclinical model of leukemia," (in eng), *Photoacoustics*, vol. 14, pp. 31-36, 2019, doi: 10.1016/j.pacs.2019.01.003.
[33] S. Cho, J. Baik, R. Managuli, and C. Kim, "3D PHOVIS: 3D photoacoustic visualization studio," *Photoacoustics*, vol. 18, p. 100168, 2020/06/01/ 2020, doi: https://doi.org/10.1016/j.pacs.2020.100168.
[34] A. T. Schäfer, "Colour measurements of pallor mortis," *International journal of legal medicine*, vol. 113, no. 2, pp. 81-83, 2000.
[35] A. Sharma , S. Srishti, V. Periyasamy, and M. Pramanik, "Photoacoustic imaging depth comparison at 532-, 800-, and 1064-nm wavelengths: Monte Carlo simulation and experimental validation," *Journal of Biomedical Optics*, vol. 24, no. 12, p. 121904, 2019. [Online]. Available: https://doi.org/10.1117/1.JBO.24.12.121904.
[36] J. R. Rajian, G. Girish, and X. Wang, "Photoacoustic tomography to identify inflammatory arthritis," *Journal of biomedical optics*, vol. 17, no. 9, p. 096013, 2012.
[37] J. R. Rajian, X. Shao, D. L. Chamberland, and X. Wang, "Characterization and treatment monitoring of inflammatory arthritis by photoacoustic imaging: a study on adjuvant-induced arthritis rat model," *Biomedical optics express*, vol. 4, no. 6, pp. 900-908, 2013.